Bioconjugate Chemistry

pubs.acs.org/bc
Article

Adapting Ferritin, a Naturally Occurring Protein Cage, to Modulate Intrinsic Agonism of OX40

Whitney Shatz-Binder,* Caleigh M. Azumaya, Brandon Leonard, Ivan Vuong, Jawahar Sudhamsu, Alexis Rohou, Peter Liu, Wendy Sandoval, Karenna Bol, Saeed Izadi, Patrick G. Holder, Craig Blanchette, Remo Perozzo, Robert F. Kelley, and Yogeshvar Kalia

Cite This: *Bioconjugate Chem.* 2024, 35, 593−603

ABSTRACT: Ferritin is a multivalent, self-assembling protein scaffold found in most human cell types, in addition to being present in invertebrates, higher plants, fungi, and bacteria, that offers an attractive alternative to polymer-based drug delivery systems (DDS). In this study, the utility of the ferritin cage as a DDS was demonstrated within the context of T cell agonism for tumor killing. Members of the tumor necrosis factor receptor superfamily (TNFRSF) are attractive targets for the development of anticancer therapeutics. These receptors are endogenously activated by trimeric ligands that occur in transmembrane or soluble forms, and oligomerization and cell-surface anchoring have been shown to be essential aspects of the targeted agonism of this receptor class. Here, we demonstrated that the ferritin cage could be easily tailored for multivalent display of anti-OX40 antibody fragments on its surface and determined that these arrays are capable of pathway activation through cell-surface clustering. Together, these results confirm the utility, versatility, and developability of ferritin as a DDS.

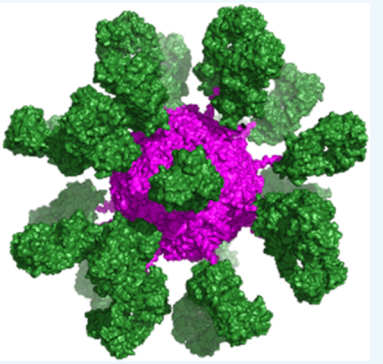

INTRODUCTION

Drug delivery systems (DDS) are becoming increasingly important in the advancement of novel therapeutics. DDS can be defined as systems that enhance therapeutic substances by modulating their pharmacokinetics (PK), toxicity, stability, or efficacy. DDS are typically leveraged for one or more of the following reasons: to enhance absorption into specific tissues, to prevent degradation in the biological environment, to improve intracellular delivery, or to control PK and drug distribution profiles. While synthetic polymeric scaffolds are commonly employed in DDS, their biocompatibility and the fate of the polymer metabolites are often of concern. On the other hand, there exist a myriad of natural polymer systems, including proteins, starch, cellulose, hyaluronic acid, and DNA which offer attractive alternatives.

Among them, protein-based nanocages such as viruses, ferritin, and others are of particular interest due to the cage-like structures being formed through self-assembly of protein subunits, which offers the advantage of being able to be made entirely recombinantly. Ferritin, a member of the iron storage family of proteins, is made up of 24 subunits held together by noncovalent interactions, arranged into an icosahedral cage with 2-, 3-, and 4-fold axes of symmetry around a central cavity.[1,2] Ferritin possesses many attractive features[3−6] as a DDS. First, it is amenable to both chemical conjugation[7−9] and molecular engineering techniques, for example, through the addition of a peptide or protein tag.[10−12] Second, ferritin is highly conserved among higher eukaryotes and therefore poses minimal risk of toxicity or immunological activity.[7] Third, because both the monomer and the assembled cage are monodisperse entities, it is simpler to analyze compared with other delivery technologies such as polydisperse polymers or liposomes. Perhaps most importantly, the multivalency of displayed amino acid side chains, either on the external surface or internally when iron is not being stored in its central cavity, endows ferritin with the potential to carry therapeutic cargo.

Members of the tumor necrosis factor receptor superfamily (TNFRSF) have long been attractive targets for the development of anticancer therapeutics. They operate in many organ systems and play a prominent role in important biological processes including regulation of immunity, cell proliferation, and cell death.[13] These receptors are endogenously activated by ligands that occur as trimeric transmembrane proteins or as soluble trimeric molecules, and oligomerization and cell-surface anchoring are known to be essential aspects of targeted agonism of this receptor class.[13−16] Because cognate ligands of these receptors have generally made suboptimal drugs due to poor production, stability, or PK, thus far, the most common therapeutic modality advanced for this receptor class has been the monoclonal antibody (mAb). However, a significant

Received: January 19, 2024
Revised: March 15, 2024
Accepted: March 26, 2024
Published: April 9, 2024

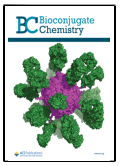

https://doi.org/10.1021/acs.bioconjchem.4c00020
Bioconjugate Chem. 2024, 35, 593−603

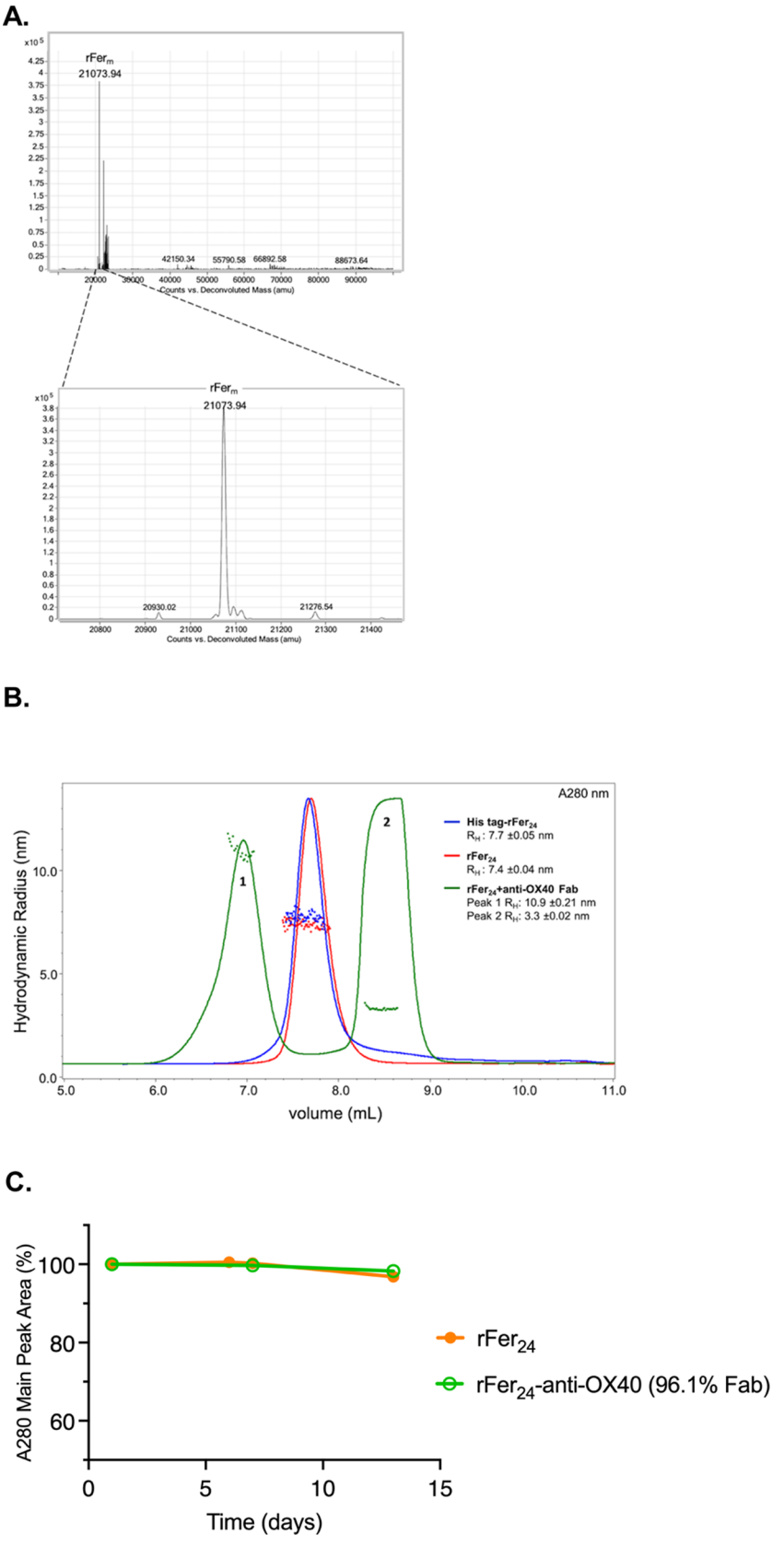

Figure 1. (A) Deconvolution from LC/MS analysis after digestion using TEV protease, with a zoomed-in view in the bottom panel. Identified masses have been assigned. (B) Size exclusion chromatography in-line with a quasi-elastic light scattering detector (SEC-QELS) of $rFer_{24}$ with His-tag (red trace) and after TEV protease digestion (blue trace), as well as $rFer_{24}$-anti-OX40 Fab conjugate (1) and unconjugated Fab (2) from reaction 1 (green trace), overlaid with measured R_H values across each peak. Averaged R_H values are also reported in the legend. (C) Physical stability profiles for $rFer_{24}$ and $rFer_{24}$-anti-OX40 Fab_{24} were measured in phosphate-buffered saline (PBS) at 25 °C over 14 days.

https://doi.org/10.1021/acs.bioconjchem.4c00020
Bioconjugate Chem. 2024, 35, 593−603

challenge for the pharmacologic agonism of these receptors by mAbs is the general requirement for receptor oligomerization or superclustering to achieve valencies beyond two.[17−19] While cross-linking of agonist anti-TNFRSF antibodies can be achieved *in vitro* by artificially coating on plates or by using secondary cross-linking reagents, *in vivo* cross-linking activity generally relies on extrinsic cross-linking from Fc engagement with Fc γ receptors (FcγRs) on immune cells.[16,20,21] This has had a significant impact on the clinical development of therapeutic antibody formats attempting to activate TNFRSFs. Despite the advancement of a large pipeline of TNFRSF agonist antibodies into development, none has been approved or reached late stage clinical trials, and several have been withdrawn.[13,14,16,22−24]

While a variety of IgG-like and non-IgG-like formats have been developed,[25] including triabodies, tetrabodies, pentabodies, self-assembling hexameric IgG antibodies, nanoparticle and cross-linked micelle conjugates,[26−31] to expand valencies beyond 2, developability considerations relating to PK, safety, and physical and chemical properties have impeded advancement of these formats to the clinic. Thus, a need for multivalent delivery strategies with favorable developability properties still exists, enabling the *in vivo* potency needed to drive clinically relevant efficacy. Since ferritin is a biocompatible, naturally occurring icosahedron, it is an attractive scaffold for multivalent engagement of TNFRSF receptors with the potential to facilitate the superclustering necessary to drive TNFRSF signaling.

In the present study, a recombinant version of the human ferritin light chain ($rFer_{24}$) was designed that includes a reactive glutamine residue embedded in a peptide sequence (Q-tag) recognized by microbial transglutaminase (mTG). In parallel, a lysine residue was embedded in an mTG-reactive peptide sequence (K-tag) into the C-terminus of the heavy chain of a recombinant anti-OX40 human IgG1 antibody fragment (Fab). Site-specific conjugation of Fab-K-tag to each ferritin monomer ($rFer_m$) containing a Q-tag proceeded through enzymatic bioconjugation catalyzed by mTG to form a Q−K isopeptide bond, resulting in a multivalent ferritin−Fab conjugate. In-depth characterization of $rFer_{24}$ and $rFer_{24}$-Fab conjugates were performed under native and denaturing conditions. The *in vitro* agonist activities of $rFer_{24}$-Fab conjugates with varying anti-OX40 Fab densities were compared to that of a previously developed IgG format that depends on extrinsic cross-linking both *in vitro* and *in vivo*. Moderate agonism was reported for a valency of 4, while highly potent activity was observed only for a hexameric IgG format, which had a valency of 12.[28] The objectives of the present study were to (i) investigate whether the $rFer_{24}$-Fab conjugate was capable of *in vitro* agonism of the OX40 pathway without relying on extrinsic cross-linking and, if so, (ii) determine how activity depends on Fab valency. Positive outcomes confirm that ferritin is a promising DDS for multivalent agonism.

RESULTS AND DISCUSSION

Results. A recombinant ferritin construct was designed with the following, starting from the N-terminus (N-term): a signal sequence for protein secretion, followed by an 8xHis tag with tobacco etch virus (TEV) protease cleavage site, followed by a microbial transglutaminase (mTG) recognition sequence (Q-tag, VLQSP)[32] with a flexible linker leading into the mature N-term of liver-derived ferritin light chain (LC) (SI.1). Following expression in Expi293 cells and Ni Sepharose excel purification, the His-tag was cleaved off using TEV protease, and the digested mixture was analyzed via liquid chromatography in-line with mass spectrometry (LC/MS) under denaturing conditions (Figure 1). As shown in Table 1, theoretical and measured masses are in good agreement with one another. Moreover, the additional minor masses visible in the top panel of Figure 1A correspond to His-tag truncations (SI.2); a phenomenon that has been observed when His-tagged proteins are expressed in mammalian cells, such as Expi293 cells.

Table 1. Theoretical and Measured Molar Masses for $rFer_m$, Anti-OX40 Fab and $rFer_m$-xOX40 Fab

	theoretical molar mass (Da)	measured molar mass (Da)	delta (Da)
8xHis-$rFer_m$	23,022.74	23,023.31	0.57
$rFer_m$	21,073.69	21,073.94	0.25
anti-OX40 Fab	47,742.28	47,742.64	0.36
$rFer_m$-xOX40	68,815.97	68,800.93	−15.04

The recombinant ferritin cage ($rFer_{24}$) was also analyzed under native conditions using size exclusion chromatography in-line with a quasi-elastic light scattering detector (SEC-QELS), both before and after cleavage of the N-term His-tag (Figure 1B, red and blue traces). As shown in the UV spectra, $rFer_{24}$ did not exhibit aggregation, with or without the His-tag. Moreover, the SEC-QELS analysis corroborated monodispersity within each pool, as demonstrated by the narrow R_H distributions across each peak.

Conjugation to $rFer_{24}$ (Q-tag, VLQSP) was accomplished using an anti-OX40 Fab with mTG amine recognition sequence (RSKLG)[33] engineered into the C-terminus (C-term) of the Fab heavy chain (HC) (Figure 2A). All mTG conjugations were set up on an $rFer_m$ basis, with initial conditions shown in Table 2 (reaction 1). SEC-QELS analysis of reaction 1 (Figure 1B, green trace) revealed a clear shift in retention time at A280 nm relative to $rFer_{24}$ (peak 1), as well as an excess of the Fab substrate (peak 2). The increased average R_H from 7.4 nm ($rFer_{24}$) and 3.3 nm (anti-OX40 Fab) to 10.9 nm also corroborated successful conjugation, while the overlaid R_Hs across peak 1 suggested that there was also some minor polydispersity within the conjugate peak. Finally, analysis of physical stability over 14 days in PBS revealed only minor changes to the main peak area, demonstrating the stability of both $rFer_{24}$ and $rFer_{24}$-anti-OX40 Fab pools at physiological pH (Figure 1C).

To gain a quantitative understanding of conjugate Fab density, an analytical reverse phase (RP) method was developed, yielding baseline resolution of $rFer_m$-Fab, Fab, and $rFer_m$ (Figure 2B). By integrating each UV peak, this method yielded a percent Fab density based on calculating the amount of Fab-modified $rFer_m$ versus unmodified $rFer_m$. With the analytical method in place, further optimization of the conjugation was accomplished by increasing the reaction concentrations of the $rFer_m$ and Fab substrates. As shown in Table 2, adjusting substrate concentrations in reaction 2 led to nearly complete saturation of conjugation sites with a calculated Fab density of 96.1% as determined by the RP method. Conjugations with different ratios of Fab to $rFer_m$ were also tested, and the resulting yields are summarized in Table 2 (reactions 3−5). In general, the targeted ratios and the resulting Fab densities were in agreement with only minor

https://doi.org/10.1021/acs.bioconjchem.4c00020
Bioconjugate Chem. 2024, 35, 593−603

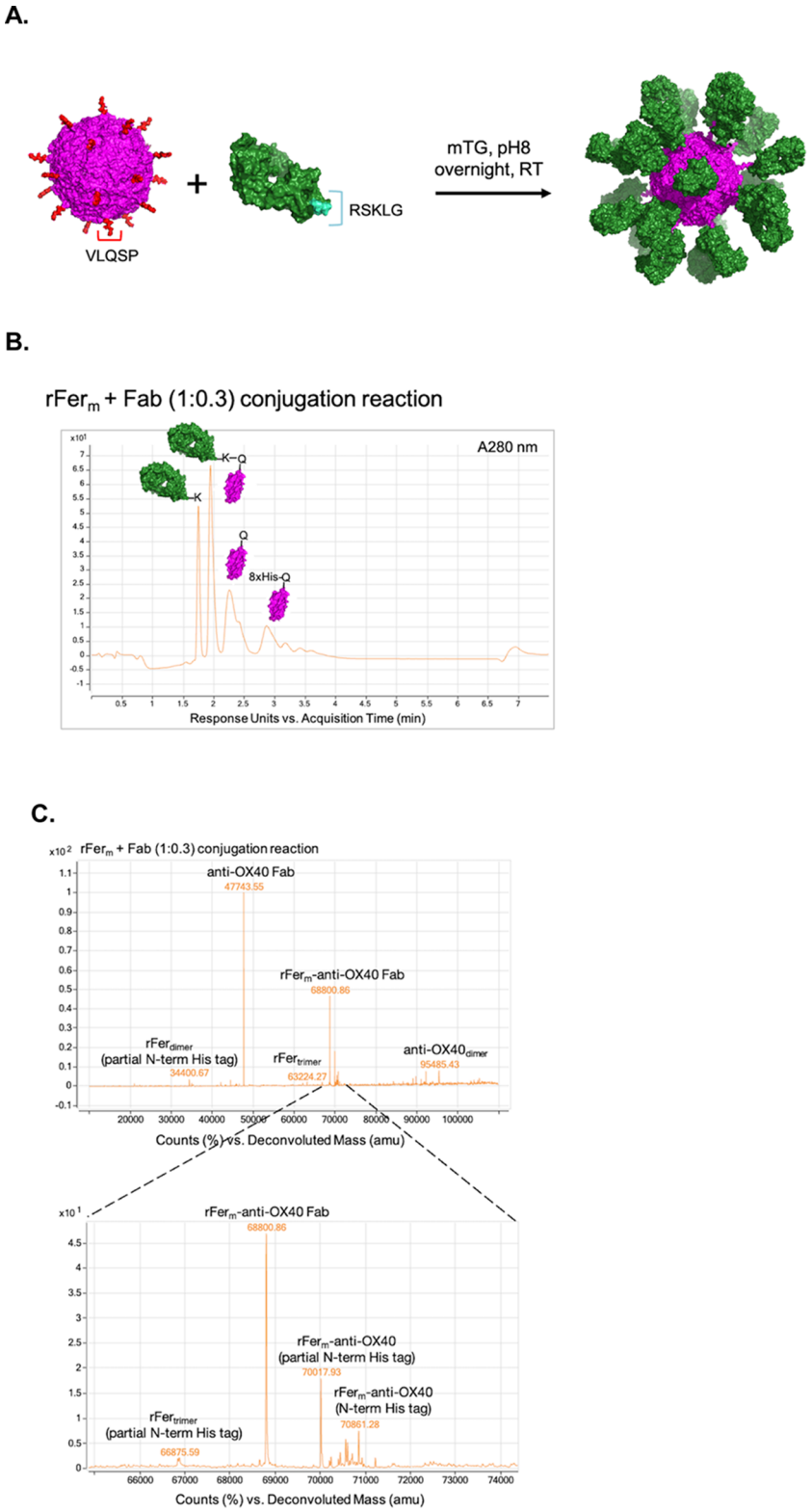

Figure 2. (A) Reaction scheme showing rFer$_{24}$ in magenta (Q-tag in red), anti-OX40 Fab (K-tag in cyan), and assembled rFer$_{24}$ + 24 Fabs. (B) Chromatogram of absorbance at 280 nm demonstrating resolution by reverse phase (RP) between unreacted anti-OX40 Fab (1.7 min), rFer$_m$-anti-OX40 Fab (2 min), rFer$_m$ (2.3 min), and rFer$_m$ with N-term His-tag (2.9 min) using a molar ratio of 1:0.3. (C) Representative deconvolution (top panel) with a zoomed-in view (bottom panel) around the mass of the rFer$_m$-anti-OX40 Fab conjugate and other minor conjugate masses.

differences. In addition to quantitation, peak identities were confirmed by deconvolution of ion count spectra using time-of-flight mass spectrometry (TOF MS), and a mass corresponding to rFer$_m$-Fab was readily detected in deconvolutions of all conjugation reactions (Table 1 and Figure 2C). Secondary conjugation products, where rFer$_m$ with a ragged N-term His-tag reacted with Fab, were also detected, suggesting that the removal of the His-tag is not necessary for the

https://doi.org/10.1021/acs.bioconjchem.4c00020
Bioconjugate Chem. 2024, 35, 593−603

Table 2. Reaction Conditions and Calculated Yields

	concn $rFer_m$ (μM)	concn Fab (μM)	concn mTG (nM)	stoichiometric ratio $rFer_m$:Fab	yield
reaction 1	50	300	350	1:6	N/D
reaction 2	350	400	350	1:1.1	96.1
reaction 3	400	200	350	1:0.5	37.6
reaction 4	400	120	350	1:0.3	19.2
reaction 5	400	80	350	1:0.2	14.2

conjugation to occur. The detection of the $rFer_m$ dimer and trimer in the deconvolutions suggest that there may also be a reactive K-site on $rFer_m$, which led to low levels of $rFer_m$ cross-linking. Overall, these results demonstrated that site occupancy could be controlled by titrating the molar ratio of Fab and that conditions could be identified that achieved nearly complete site occupancy (96.1%). To further confirm site-specific conjugation, the $rFer_{24}$-anti-OX40 Fab_{24} conjugate was also assessed by peptide mapping, and site-specific addition of K from the Fab to Q from $rFer_m$ was the predominant peptide mass detected (S1.3 and Table S1).

To gain a better understanding of spatial distribution, a $rFer_{24}$-Fab_{24} homology model was constructed, including 24 Fabs with site-specific isopeptide bond formation (Figure 3).

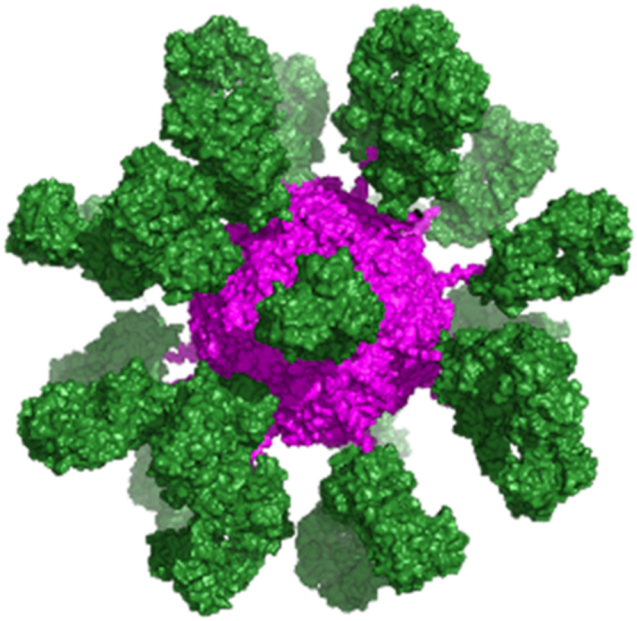

Figure 3. PYMOL rendering of $rFer_{24}$-anti-OX40 Fab_{24} from the homology model PDB file, where the $rFer_{24}$ cage is in magenta and 24 repeats of the Fab moiety are in green.

Visualization of assembled $rFer_{24}$-Fab_{24} gives a good sense of the spatial packing of the Fabs decorating the surface of the $rFer_{24}$ cage. Moreover, $rFer_{24}$-Fab_{24} was also analyzed using negative stain and cryo-EM (Figures 4 and S4). Clear, high-resolution density can be seen for the $rFer_{24}$ cage in both negative stain and cryo-EM class averages, suggesting that the cage is intact and stable. On the other hand, as shown in Figure 4, the Fabs are blurred in the averages indicating that they are flexibly linked to the $rFer_{24}$, with much conformational freedom. Furthermore, using back projections of the homology model allowed for comparison of two-dimensional (2D) particle topography with the 2D averages calculated from the negative stain and cryo-EM data. Together these results give further insight into the morphology of the DDS. They also validate the suitability of this approach for multivalent conjugation by demonstrating that $rFer_{24}$ is amenable to site-specific addition of up to 24 Fabs and that the resulting conjugate can be developed for therapeutic applications requiring multivalency.

Finally, anti-OX40 formats were tested for their ability to promote receptor signaling using engineered Jurkat cells expressing human OX40 and an NF-κB luciferase reporter (Figure 5). While cross-linking the natural ligand with a secondary antibody (OX40L-Fc XL) resulted in potent receptor activation, monovalent anti-OX40 Fab or bivalent anti-OX40 IgG1 failed to agonize OX40. In contrast, all ratios of $rFer_{24}$-Fab led to receptor activation. At the highest Fab density ($rFer_{24}$-anti-OX40 Fab with 96.1% Fab density), agonism was comparable to that of the Fab density of the OX40L-Fc XL and did not exhibit the pronounced decrease in activity observed for OX40L-Fc XL at higher concentrations. In addition, the lower Fab:$rFer_{24}$ ratios demonstrated that potency is dependent on the Fab density and highlighted the ability of the $rFer_{24}$ cage to titrate agonism. Finally, it should be noted that $rFer_{24}$ without conjugated Fab did not produce any activity.

DISCUSSION

Several ferritin-based vaccines are in clinical trials,[34] and ferritin is also in-use for delivery of chemotherapy, immunotherapy and imaging.[35−37] The work presented here extends its use cases to another therapeutic setting through the multivalent display of Fabs to induce agonism through receptor superclustering. As a recombinant protein, $rFer_{24}$ was amenable to protein engineering, where an amino acid sequence for site-specific conjugation was fused onto the $rFer_m$ N-terminus. Native analysis of the $rFer_{24}$ substrate by SEC-QELS also confirmed a well-behaved, monodispersed protein. In addition, mTG was effective at catalyzing the formation of isopeptide bonds between Q on $rFer_{24}$ and K on anti-OX40 Fab (Figures 1B, 2B,C, and SI.2). While initial conditions were able to produce the $rFer_{24}$-Fab conjugate, further optimization of molar concentrations of each substrate led to a decrease in the Fab ratio (Table 2). This finding is likely related to the fact that mTG conjugation is K_m-driven, and thus, in addition to stoichiometry, the concentration of each substrate plays a role in conjugation efficiency. Finally, the lack of major aggregation suggests that $rFer_{24}$-anti-OX40 Fab is a stable, well-behaved molecule with a high potential for developability (Figure 1C).

To demonstrate that all 24 $rFer_m$ subunits were occupied by Fab, a RP method was established to quantitatively determine the amount of Fab-modified $rFer_m$ per cage (Figure 2B) and the results confirmed that nearly all 24 rFer monomers were conjugated to Fab, with 96.1% Fab coverage under optimal conditions (Table 2). We also determined that $rFer_{24}$ with various ratios of Fab displayed on the surface could be assembled by controlling the stoichiometry (Table 2). Traditional analytical techniques were sufficient to demonstrate a well-behaved conjugate with minimal secondary cross-linking (Figure 2C, SI.3. Table S1). While the LC/MS deconvolution revealed heterogeneity of the N-term of $rFer_m$, it also demonstrated that this heterogeneity did not interfere with reactivity since all forms of $rFer_{24}$ were able to react with Fab, as indicated by the resulting conjugate masses (Figure 2C).

https://doi.org/10.1021/acs.bioconjchem.4c00020
Bioconjugate Chem. 2024, 35, 593−603

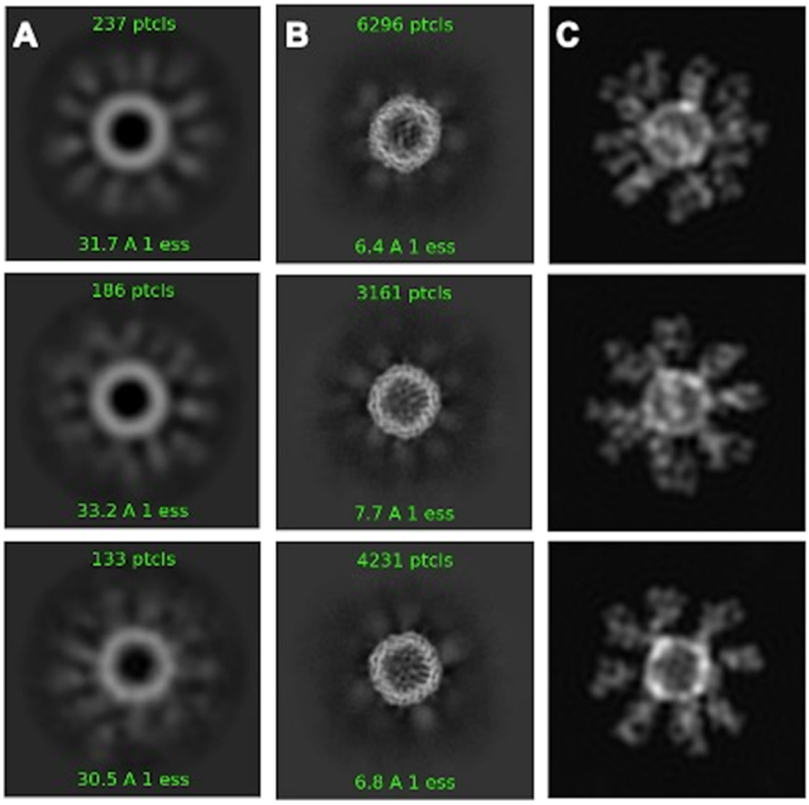

Figure 4. (A) Representative 2D class averages of negatively stained rFer-OX40 and Fab_{24} conjugates. (B) Representative 2D class averages of rFer-OX40 Fab particles were imaged using cryo-EM. (C) Back projections of the homology model are presented in Figure 3.

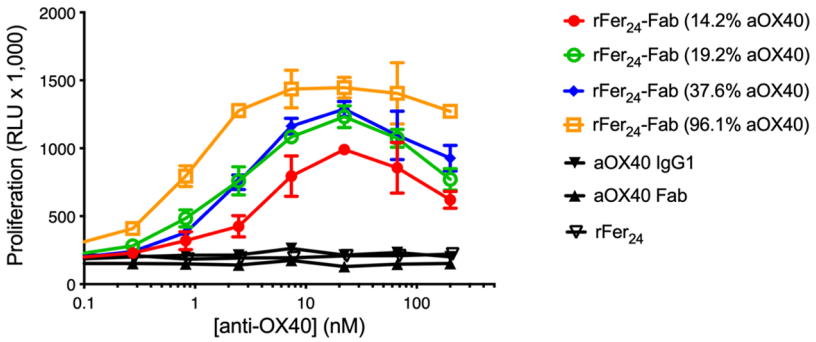

Figure 5. OX40+ Jurkat reporter assay. RLU denotes relative luminescence. Molecule concentrations (nM) were calculated as follows: $rFer_{24}$-Fab conjugate and aOX40 Fab concentrations were based on Fab molar mass, OX40L-Fc XL concentration was based on OX40L-Fc XL molar mass, aOX40 IgG1 concentration was based on the antibody molar mass, and $rFer_{24}$ concentration was based on the molar mass of the assembled ferritin cage.

Molecular modeling indicates that the assembly of 24 Fabs onto the $rFer_{24}$ scaffold is sterically possible, with enough inter-Fab distance to accommodate conformational changes (Figure 3). To build the homology model, the Fabs were manually placed near the engineered sequence for isopeptide bond creation; therefore, the current representation of the system is not necessarily energetically realistic. Interdomain interactions such as pH-dependent electrostatic and van der Waals interactions between the Fab domain could induce conformational changes limiting the accessibility of conjugation sites and could also impact the dynamics of the Fabs, potentially influencing oligomerization or superclustering. Due to the large size of the system (number of atoms >300 K), a thorough yet practical analysis of these effects requires coarse-grained modeling[38] or atomistic multiscale modeling using implicit solvent models,[39] which are beyond the current scope of our study. Nevertheless, the current model confirms the viability of spatial arrangement of the Fabs around $rFer_{24}$ with enough inter-Fab distances to allow conformational flexibility, as supported by the negative stain and cryo-EM data.

Indeed, the negative stain and cryo-EM micrographs allowed for further understanding of the overall morphology of the system (Figures 4 and S4) and confirmed the validity of the homology model. The stark contrast in resolution between the $rFer_{24}$ cage and the surrounding Fabs suggests that while the cage is in a relatively rigid conformation, the Fabs are able to move around in a variety of orientations. Moreover, back projections of the homology model allowed comparison with the 2D averages calculated from the negative stain and cryo-EM data. Although not well resolved due to their flexibility, the

https://doi.org/10.1021/acs.bioconjchem.4c00020
Bioconjugate Chem. 2024, 35, 593−603

number of apparent Fab densities in the averages is reasonable compared to the number of Fab densities that are seen in different views of the homology model. This finding gives further insight into the conformational flexibility of the Fab domains when conjugated to the $rFer_{24}$ cage.

Overall, the robust activity of the conjugates demonstrates the ability of the multivalent array to take the nonfunctional Fab and turn it into one with high activity once displayed on the $rFer_{24}$ cage. This highlights the value of the $rFer_{24}$ cage as a DDS, which was amenable to addition of the TG recognition sequence and was able to accommodate the display of up to 24 Fabs on its surface. Furthermore, different ratios of $rFer_{24}$-anti-OX40 Fab conjugates were tested for their ability to promote receptor signaling using engineered Jurkat cells expressing human OX40 and an NF-κB luciferase reporter (Figure 5). While cross-linking the natural ligand with a secondary antibody (OX40L-Fc XL) resulted in potent receptor activation, monovalent anti-OX40 Fab or bivalent anti-OX40 IgG1 failed to agonize OX40. In contrast, all ratios of $rFer_{24}$-anti-OX40 Fab led to receptor activation. At the highest Fab occupancy, agonism was comparable to that of the OX40L-Fc XL. Interestingly, the hook effect that was observed with the OX40L-Fc XL at Fab concentrations greater than 20 nM was less pronounced with the $rFer_{24}$-anti-OX40 Fab conjugates. This decrease in activity at high OX40L-Fc XL concentrations suggests that topology may play a role in agonizing the receptor pathway. At low-to-moderate OX40L-Fc XL concentrations, it is likely that one trimeric ligand is bound to multiple receptors, whereas at high OX40L-Fc XL, it is more likely that only one receptor is bound to each trimeric ligand, leading to less potent signaling compared to the $\geq$2 receptors per complex case. In contrast, we hypothesize that although the anti-OX40 Fabs maintain a high degree of conformational freedom, their colocalization on the $rFer_{24}$ cage impacts their interaction with the receptors by enabling a single $rFer_{24}$-Fab array to cluster multiple receptors at higher molar concentrations than for OX40L-Fc XL. These observed differences suggest that geometry may play a role in pathway activation where colocalization of Fabs on the same scaffold may enhance clustering of OX40 receptors at saturating receptor concentrations. Moreover, the modulation of activity based on Fab percent occupancy was also demonstrated, highlighting the ability of the $rFer_{24}$ cage to titrate agonism. Although, it was surprising to observe that $rFer_{24}$-anti-OX40 (96.1% Fab) did not lead to agonism any greater than that of the cross-linked trimer, despite presenting up to 4 times as much Fab per molecule, this is attributed to reaching the upper limit of the assay range.

Overall, this study demonstrates the suitability of the $rFer_{24}$ DDS for the pharmacologic agonism of this important therapeutic target class. Because cognate ligands of these receptors have generally made suboptimal drugs due to poor production, stability, or PK and mAbs have failed in the clinic due to a lack of efficacy, the $rFer_{24}$ DDS constitutes a promising platform for multivalent delivery of Fabs. While therapeutic validation requires *in vivo* studies, this work corroborates previous proof-of-concept studies[27,28] and further establishes the general utility of the ferritin cage as a DDS.

MATERIALS AND METHODS

Construct Design and Expi/293T Expression and Purification. A light chain ferritin sequence derived from human liver ferritin was used to produce the recombinant ferritin (rFer) construct, based on a standard pRK vector with the protein cloned into BamH1 and EcoR1 sites.[40,41] The N-terminus of the construct contained an 8xHis tag, followed by a tobacco etch virus (TEV) protease cleavage site, followed by VLQSPGGSGGGSG. This sequence was designed to be recognized by microbial transglutaminase (mTG), which catalyzes the formation of an isopeptide bond between the glutamine in the sequence and a lysine substrate (Figure 1).

Expression was done in Expi/293T cells (Thermo Fisher) at the 4 L scale for 14 days. Secretion medium was harvested and passed over a 5 mL column packed with Ni Sepharose excel (Millipore Sigma) using a running buffer consisting of 50 mM NaH_2PO_4, 200 mM NaCl, pH 8.0, spiked with 10 mM imidazole. Following on-column washing, an elution buffer consisting of the running buffer spiked with 400 mM imidazole was applied, and 1 mL fractions were collected.

TEV Protease Cleavage. The N-term His-tag was removed using a TEV protease (ATCC) at a ratio of 1:80 w/w. The digestion pool was held at room temperature for 5 h, followed by a flow through purification using a 5 mL Ni excel column to remove undigested protein as well as TEV protease. The protein pool was then dialyzed against PBS 7.4 and stored at 4 °C.

Fabs for Microbial Transglutaminase (mTG) Conjugation. The C-terminus of a Fab heavy chain was engineered to contain lysine (Lys) in a consensus sequence (RSKLG) for mTG conjugation to an anti-OX40 Fab targeting an extracellular domain (ECD) of human OX40R.

Microbial TG Chemistry. A microbial TG enzyme (mTG) derived from *Streptomyces mobaraensis* was used to catalyze isopeptide bond formation between Q from rFer and K from Fab, where each substrate contained a specific recognition motif designed based on previously described sequences.[32] In this case, rFer was engineered to contain the N-term consensus sequence VLQSP, while Fab was engineered to contain the C-terminal sequence RSKLG. Reaction stoichiometry was calculated on a ferritin monomeric subunit basis ($rFer_m$), as listed in Table 2. All Reactions were titrated to pH 8.0 using 1 M Tris and allowed to incubate for 18−24 h at room temperature. Following conjugation, unreacted Fab was removed by SEC (S400, 10 × 300 mm).

SEC-QELS. Determination of purity and R_H of rFer proteins and conjugates under native conditions was accomplished using SEC-QELS using an Acclaim SEC-1000 analytical SEC column run on a Dionex UltiMate 3000 UHPLC (Thermo Fisher Scientific) with isocratic elution in phosphate-buffered saline (PBS) spiked with an additional 150 mM NaCl. In-line with UV detection, a multiangle laser light scattering detector (MALS detector, Wyatt Instruments) was used to determine molar mass due to Brownian motion, as well as an attached photon-counting module (QELS detector, Wyatt Instruments) to capture fluctuations in intensity of scattered laser light, allowing diffusion coefficients to be measured. Assuming a spherical shape, the Stokes−Einstein relationship was used to calculate R_H from D.

Stability. Physical stability was analyzed by incubating $rFer_{24}$ and $rFer_{24}$-anti-OX40 Fab cells in PBS at room temperature for 14 days. At each time point, 50 μg of each sample was run on SEC (same conditions as for SEC-MALS) and the percent main peak area was calculated by compared to the peak area on day 1.

RP-MS. RP-MS was used to determine the $rFer_m$:Fab ratios. For all gradients, mobile phase A consisted of 0.05%

https://doi.org/10.1021/acs.bioconjchem.4c00020
Bioconjugate Chem. 2024, 35, 593−603

trifluoroacetic acid (TFA) in water, while mobile phase B consisted of 0.05% TFA and 100% acetonitrile (ACN). Resolution of rFer, $rFer_m$-Fab conjugates and impurities was accomplished using a reverse phase (RP) C4 column (Waters, Acquity HPLC Protein BEH C4, 2 × 150 mm), consisting of a hydrophobic alkyl chain in the stationary phase. The number of Fabs per $rFer_{24}$ cage was determined by quantifying the amount of unconjugated, free $rFer_m$ using a standard curve from UV280 peak integrations of unmodified $rFer_m$ on RP. The concentration of $rFer_m$-Fab was then calculated using eq 1

$$[rFer_mFab] = \frac{(\text{total OD} - [rFer_m] \times 0.74)}{1.12} \quad (1)$$

where 0.74 is the calculated extinction coefficient of $rFer_m$ and 1.12 is the extinction coefficient for $rFer_m$-Fab. The percentage of $rFer_m$-Fab conjugates (% Fab) was determined by using eq 2.

$$\%\ \text{Fab} = \frac{[rFer_mFab]}{[rFer_mFab] + [rFer_m]} \times 100 \quad (2)$$

In addition, mass data were acquired as described previously[32] using an Agilent 1290 Infinity HPLC in tandem with an Agilent 6230 ESI/TOF mass spectrometer, operating in positive ion mode.

Peptide Mapping. To prepare samples for peptide mapping, 10 μg of sample was denatured using 8 M guanidine hydrochloride (GuHCl), reduced using DTT and alkylated using iodoacetamide (IAA), followed by trypsin digestion at 37 °C overnight. The samples were loaded on a desalting column (Pierce C18 Spin Tips) for the removal of impurities. Five percent of each digest was injected onto a LTQ-Orbitrap Elite MS spectrometer coupled with a nanoAcquity HPLC (Waters). Raw data were searched with Byonic and analyzed by Byologic using semitryptic search, Fixed Mod: Carbam (Cys) and Variable Mod: Oxidation (Met, pyroGln(N-term)); Cross-linked (−17.031 Da) (Lys/Gln).

Molecular Modeling. Conjugates of ferritin and anti-OX40 Fab were the components used for the molecular modeling. To begin, Human L ferritin in the PDB format (5LG8) was imported into the Molecular Operation Environment (MOE) software. The "Protein Builder" tool was used to prepend the engineered sequence to the N-terminus of each subunit. The same tool was then used to mutate the amino acids in the ferritin sequence to match those used in the experiment. The anti-OX40 Fab structure was predicted from its sequence using the antibody modeler within MOE. Twenty-four copies of the fab homology model were imported along with the ferritin structure. The "Render" tool was used to visualize the molecules in the Q residue near the N-term of the ferritin subunits and the K residue near the C-term of the anti-OX40 Fab. Each one of the 24 Fabs were selected and manually placed in proximity to the engineered sequence on the N-terminus of a ferritin subunit. The Fabs were positioned so that the terminus side chains were in the proximity to form a covalent bond. The "Molecule Builder" feature was then used to remove the amine group of the Q residue. The adjacent carbon and nitrogen on the K side chain were selected, and a bond was introduced using the Molecule Builder. This was repeated 24 times for each Fab and ferritin subunit. The system was then energy-minimized in MOE, and the PDB structure was ready to remove any local steric clashes. However, a global conformational relaxation requires extended molecular simulations, which was not pursued. Because the Fabs were manually moved into the proximity of the engineered N-term $rFer_{24}$ sequence to create the isopeptide bond, the secondary structure of the peptides in this region as well as the arrangement of the atoms in the isopeptide bond are not conformationally accurate.

Negative Stain Sample Preparation. The $rFer_{24}$-Fab_{24} sample was diluted 1:100 to a concentration of 0.03 mg/mL. 400 mesh copper, continuous-carbon/Formvar grids (Ted Pella) were used and 4 μL of sample was applied to a glow-discharged (30 s, 30 mA on GloCube) grid for 30 s before being washed two times with water and then two times with 2% uranyl acetate solution. Grids were dried before imaging.

Negative Stain Data Collection. 78 negative stain micrographs were collected using a Ceta 16 M camera on a Talos 200 kV side entry microscope (Thermo Fisher). SerialEM[42] was used for semiautomated data collection with nominal defocus between −2.0 and −3.0 μm.

Negative Stain Data Processing. 78 micrographs were imported into cryoSPARC version 4.4.0[43] and CTF-corrected using CTFFIND4,[44] and 62 particles were manually picked and averaged into 5 classes. Two of these class averages were used for a template pick, and 4600 putative particles were extracted for 2D classification. Two rounds of selection were performed to reduce the number of picks to 3978 particles classified into 50 classes.

Cryo-EM Sample Preparation. The $rFer_{24}$-Fab_{24} conjugate sample was diluted to 0.75 mg/mL. UltrAufoil 200 mesh 2/2 grids were coated in self-assembled monolayers[45] and double-blotted using a Vitrobot MARK IV (Thermo Fisher) for 3 s at 7 force. Grids were clipped for use with a Thermo Fisher autoloader (Nanosoft).

Cryo-EM Data Collection. 10,115 micrographs were collected on a Krios G3i microscope (Thermo Fisher) with a BioQuantum energy filter and K3 camera (Gatan). Data were collected semiautomatically using a SerialEM[42] image shift pattern of 6 images per hole in a 3 × 3 pattern. Nominal defocus was set to −0.8 to −1.8 μm.

Cryo-EM Data Processing. Cryo-EM data were transferred, patch motion-corrected, patch CTF-estimated, blob picked, and extracted in a 512-pixel box binned to 324 pix. 950,000 putative particles were picked. After three rounds of 2D classification and selection, 635,876 particles were classified in 2D for final 2D averages. $rFer_{24}$ was easily reconstructed to the Nyquist limit of 2.69A, but the Fabs were bound too flexibly to average into any clear density. All processing was done in cryoSPARC 4.4.0.[43] The $rFer_{24}$-Fab_{24} conjugate was opened in ChimeraX,[46] converted into an mrc, and resampled on a map from the cryo-EM data. This volume was loaded into cryoSPARC to be back-projected in 2D in order to compare with the 2D class averages from the data collected here.

OX40+ Jurkat Reporter Assay. OX40L protein extracellular domain (ECD) fused to the fragment crystallizable (Fc) region of human IgG1 (OX40L-Fc) was obtained from Sino Biological (13127-H01H). Extrinsic cross-linking of OX40L-Fc (OX40L-Fc XL) was accomplished using goat antihuman IgG Fcγ fragment specific antibody (Jackson ImmunoResearch Laboratories Inc., 109-005-098) at a final concentration of 10 μg/mL.

Anti-OX40 IgG1, OX40-Fc XL, and rFer-Fab conjugates were serially diluted 2-fold in AIM-V media (Thermo Fisher Scientific, 12055-091), and 20 μL of each diluted anti-OX40 format was added to a well in a 384-well tissue culture plates

https://doi.org/10.1021/acs.bioconjchem.4c00020
Bioconjugate Chem. 2024, 35, 593−603

(Corning Inc., 3985BC) where OX40-overexpressing Jurkat cells engineered with an NFκB luciferase reporter had been seeded at a density of 80,000 cells/well in 20 μL AIM-V media. The treated cells were incubated for 16−18 h at 37 °C and 5% CO_2 with 95% relative humidity. Following incubation, 40 μL Bright Glo (Promega, E2610) was added and mixed at room temperature for 10 min. Luminescence was detected on an Infinite M1000 Pro plate reader (Tecan).

■ ASSOCIATED CONTENT

Supporting Information

The Supporting Information is available free of charge at https://pubs.acs.org/doi/10.1021/acs.bioconjchem.4c00020.

Plasmid sequence for liver-derived ferritin LC; full deconvoluted spectrum of $rFer_m$; peptide mapping of isopeptide bond between $rFer_m$ and anti-OX40 Fab and accompanying table with detected peptides; and representative micrographs, raw particles, and class averages of $rFer_{24}$-anti-OX40 Fab_{24} conjugate in negative stain and cryo-EM (PDF)

■ AUTHOR INFORMATION

Corresponding Author

Whitney Shatz-Binder − *Protein Chemistry, Genentech Inc., South San Francisco, California 94080, United States; Pharmaceutical Sciences, University of Geneva, Geneva 1211, Switzerland;* orcid.org/0000-0003-2996-501X; Email: shatz.whitney@gene.com

Authors

Caleigh M. Azumaya − *Structural Biology, Genentech Inc., South San Francisco, California 94080, United States;* orcid.org/0000-0002-3484-9921

Brandon Leonard − *Antibody Engineering, Genentech Inc., South San Francisco, California 94080, United States*

Ivan Vuong − *Protein Chemistry, Genentech Inc., South San Francisco, California 94080, United States; Pritzker School of Molecular Engineering, University of Chicago, Chicago, Illinois 60637, United States*

Jawahar Sudhamsu − *Structural Biology, Genentech Inc., South San Francisco, California 94080, United States*

Alexis Rohou − *Structural Biology, Genentech Inc., South San Francisco, California 94080, United States;* orcid.org/0000-0002-3343-9621

Peter Liu − *Microchemistry, Proteomics and Lipidomics, Genentech Inc., South San Francisco, California 94080, United States*

Wendy Sandoval − *Microchemistry, Proteomics and Lipidomics, Genentech Inc., South San Francisco, California 94080, United States*

Karenna Bol − *Pharmaceutical Chemistry and Business and Program Management, Genentech Inc., South San Francisco, California 94080, United States*

Saeed Izadi − *Pharmaceutical Chemistry, Genentech Inc., South San Francisco, California 94080, United States*

Patrick G. Holder − *Protein Chemistry, Genentech Inc., South San Francisco, California 94080, United States;* orcid.org/0000-0003-0971-191X

Craig Blanchette − *Protein Chemistry, Genentech Inc., South San Francisco, California 94080, United States*

Remo Perozzo − *Pharmaceutical Sciences, University of Geneva, Geneva 1211, Switzerland*

Robert F. Kelley − *Pharmaceutical Chemistry, Genentech Inc., South San Francisco, California 94080, United States;* orcid.org/0000-0002-2103-3931

Yogeshvar Kalia − *Pharmaceutical Sciences, University of Geneva, Geneva 1211, Switzerland;* orcid.org/0000-0001-9049-5489

Complete contact information is available at: https://pubs.acs.org/10.1021/acs.bioconjchem.4c00020

Funding

Funding for this project was provided by Genentech Inc.

Notes

The authors declare no competing financial interest.

Notes All authors are current or former employees of Genentech, a member of the Roche Group, and are shareholders in Roche. This study was supported by internal Genentech funds, and the funders had no role in study design, data collection and analysis, decision to publish, or preparation of the manuscript.

■ ACKNOWLEDGMENTS

Yanli Yang, Greg Lazar, Christine Huang, Yavuz Dagdas, Eric Day, Devin Tesar, Sreedhara Alavattam.

■ REFERENCES

(1) Harrison, P. M. The Structure and Function of Ferritin. *Biochem. Educ.* **1986**, *14* (4), 154−162.

(2) Harrison, P. M.; Arosio, P. The Ferritins: Molecular Properties, Iron Storage Function and Cellular Regulation. *Biochim. Biophys. Acta, Bioenerg.* **1996**, *1275* (3), 161−203.

(3) Li, J. Y.; Paragas, N.; Ned, R. M.; Qiu, A.; Viltard, M.; Leete, T.; Drexler, I. R.; Chen, X.; Sanna-Cherchi, S.; Mohammed, F.; Williams, D.; Lin, C. S.; Schmidt-Ott, K. M.; Andrews, N. C.; Barasch, J. Scara5 Is a Ferritin Receptor Mediating Non-Transferrin Iron Delivery. *Dev. Cell* **2009**, *16* (1), 35−46.

(4) Li, L.; Fang, C. J.; Ryan, J. C.; Niemi, E. C.; Lebrón, J. A.; Björkman, P. J.; Arase, H.; Torti, F. M.; Torti, S. V.; Nakamura, M. C.; Seaman, W. E. Binding and Uptake of H-Ferritin Are Mediated by Human Transferrin Receptor-1. *Proc. Natl. Acad. Sci. U.S.A.* **2010**, *107* (8), 3505−3510.

(5) Zhang, S.; Zang, J.; Chen, H.; Li, M.; Xu, C.; Zhao, G. The Size Flexibility of Ferritin Nanocage Opens a New Way to Prepare Nanomaterials. *Small* **2017**, *13* (37), No. 1701045.

(6) He, D.; Marles-Wright, J. Ferritin Family Proteins and Their Use in Bionanotechnology. *New Biotechnol.* **2015**, *32* (6), 651−657.

(7) Kanekiyo, M.; Wei, C.-J.; Yassine, H. M.; McTamney, P. M.; Boyington, J. C.; Whittle, J. R. R.; Rao, S. S.; Kong, W.-P.; Wang, L.; Nabel, G. J. Self-Assembling Influenza Nanoparticle Vaccines Elicit Broadly Neutralizing H1N1 Antibodies. *Nature* **2013**, *499* (7456), 102−106.

(8) Lin, C.-Y.; Yang, S.-J.; Peng, C.-L.; Shieh, M.-J. Panitumumab-Conjugated and Platinum-Cored PH-Sensitive Apoferritin Nanocages for Colorectal Cancer-Targeted Therapy. *ACS Appl. Mater. Inter.* **2018**, *10* (7), 6096−6106.

(9) Wei, J.; Li, Z.; Yang, Y.; Ma, G.; Su, Z.; Zhang, S. An Apoferritin−Hemagglutinin Conjugate Vaccine with Encapsulated Nucleoprotein Antigen Peptide from Influenza Virus Confers Enhanced Cross Protection. *Bioconjugate Chem.* **2020**, *31* (8), 1948−1959.

(10) Hooker, J. M.; Datta, A.; Botta, M.; Raymond, K. N.; Francis, M. B. Magnetic Resonance Contrast Agents from Viral Capsid Shells: A Comparison of Exterior and Interior Cargo Strategies. *Nano Lett.* **2007**, *7* (8), 2207−2210.

(11) Wang, C.; Zhang, C.; Li, Z.; Yin, S.; Wang, Q.; Guo, F.; Zhang, Y.; Yu, R.; Liu, Y.; Su, Z. Extending Half Life of H-Ferritin

Nanoparticle by Fusing Albumin Binding Domain for Doxorubicin Encapsulation. *Biomacromolecules* **2018**, *19* (3), 773−781.
(12) Su, W.; Tan, H.; Janowski, R.; Zhang, W.; Wang, P.; Zhang, J.; Zhai, H.; Li, J.; Niessing, D.; Sattler, M.; Zou, P. Ferritin-Displayed GLP-1 with Improved Pharmacological Activities and Pharmacokinetics. *Mol. Pharmaceutics* **2020**, *17* (5), 1663−1673.
(13) Sturgill, E. R.; Redmond, W. L. TNFR Agonists: A Review of Current Biologics Targeting OX40, 4-1BB, CD27, and GITR. *Am. J. Hematol./Oncol.* **2017**, *13* (11), 4−15.
(14) Croft, M.; Benedict, C. A.; Ware, C. F. Clinical Targeting of the TNF and TNFR Superfamilies. *Nat. Rev. Drug Discovery* **2013**, *12* (2), 147−168.
(15) Faustman, D. L.; Davis, M. TNF Receptor 2 and Disease: Autoimmunity and Regenerative Medicine. *Front. Immunol.* **2013**, *4*, 478.
(16) Mayes, P. A.; Hance, K. W.; Hoos, A. The Promise and Challenges of Immune Agonist Antibody Development in Cancer. *Nat. Rev. Drug Discovery* **2018**, *17* (7), 509−527.
(17) Vanamee, É. S.; Faustman, D. L. Structural Principles of Tumor Necrosis Factor Superfamily Signaling. *Sci. Signaling* **2018**, *11* (511), No. eaao4910, DOI: 10.1126/scisignal.aao4910.
(18) Wajant, H. Principles of Antibody-Mediated TNF Receptor Activation. *Cell Death Differ.* **2015**, *22* (11), 1727−1741.
(19) Holler, N.; Tardivel, A.; Kovacsovics-Bankowski, M.; Hertig, S.; Gaide, O.; Martinon, F.; Tinel, A.; Deperthes, D.; Calderara, S.; Schulthess, T.; Engel, J.; Schneider, P.; Tschopp, J. Two Adjacent Trimeric Fas Ligands Are Required for Fas Signaling and Formation of a Death-Inducing Signaling Complex. *Mol. Cell. Biol.* **2003**, *23* (4), 1428−1440.
(20) Furness, A. J. S.; Vargas, F. A.; Peggs, K. S.; Quezada, S. A. Impact of Tumour Microenvironment and Fc Receptors on the Activity of Immunomodulatory Antibodies. *Trends Immunol.* **2014**, *35* (7), 290−298.
(21) Wilson, N. S.; Yang, B.; Yang, A.; Loeser, S.; Marsters, S.; Lawrence, D.; Li, Y.; Pitti, R.; Totpal, K.; Yee, S.; Ross, S.; Vernes, J.-M.; Lu, Y.; Adams, C.; Offringa, R.; Kelley, B.; Hymowitz, S.; Daniel, D.; Meng, G.; Ashkenazi, A. An Fcγ Receptor-Dependent Mechanism Drives Antibody-Mediated Target-Receptor Signaling in Cancer Cells. *Cancer Cell* **2011**, *19* (1), 101−113.
(22) Ashkenazi, A. Targeting the Extrinsic Apoptotic Pathway in Cancer: Lessons Learned and Future Directions. *J. Clin. Invest.* **2015**, *125* (2), 487−489.
(23) Bremer, E. Targeting of the Tumor Necrosis Factor Receptor Superfamily for Cancer Immunotherapy. *ISRN Oncol.* **2013**, *2013*, No. 371854.
(24) Chester, C.; Ambulkar, S.; Kohrt, H. E. 4-1BB Agonism: Adding the Accelerator to Cancer Immunotherapy. *Cancer Immunol. Immunother.* **2016**, *65* (10), 1243−1248.
(25) Steeland, S.; Vandenbroucke, R. E.; Libert, C. Nanobodies as Therapeutics: Big Opportunities for Small Antibodies. *Drug Discovery Today* **2016**, *21* (7), 1076−1113.
(26) Cuesta, Á. M.; Sainz-Pastor, N.; Bonet, J.; Oliva, B.; Álvarez-Vallina, L. Multivalent Antibodies: When Design Surpasses Evolution. *Trends Biotechnol.* **2010**, *28* (7), 355−362.
(27) Nuñez-Prado, N.; Compte, M.; Harwood, S.; Álvarez-Méndez, A.; Lykkemark, S.; Sanz, L.; Álvarez-Vallina, L. The Coming of Age of Engineered Multivalent Antibodies. *Drug Discovery Today* **2015**, *20* (5), 588−594.
(28) Yang, Y.; Yeh, S. H.; Madireddi, S.; Matochko, W. L.; Gu, C.; Sanchez, P. P.; Ultsch, M.; Boenig, G. D. L.; Harris, S. F.; Leonard, B.; Scales, S. J.; Zhu, J. W.; Christensen, E.; Hang, J. Q.; Brezski, R. J.; Marsters, S.; Ashkenazi, A.; Sukumaran, S.; Chiu, H.; Cubas, R.; Kim, J. M.; Lazar, G. A. Tetravalent Biepitopic Targeting Enables Intrinsic Antibody Agonism of Tumor Necrosis Factor Receptor Superfamily Members. *mAbs* **2019**, *11* (6), 996−1011.
(29) Darwish, M.; Shatz, W.; Leonard, B.; Loyet, K.; Barrett, K.; Wong, J. L.; Li, H.; Abraham, R.; Lin, M.; Franke, Y.; Tam, C.; Mortara, K.; Zilberleyb, I.; Blanchette, C. Nanolipoprotein Particles as a Delivery Platform for Fab Based Therapeutics. *Bioconjugate Chem.* **2020**, *31* (8), 1995−2007.
(30) Florinas, S.; Liu, M.; Fleming, R.; Vlerken-Ysla, L. V.; Ayriss, J.; Gilbreth, R.; Dimasi, N.; Gao, C.; Wu, H.; Xu, Z.-Q.; Chen, S.; Dirisala, A.; Kataoka, K.; Cabral, H.; Christie, R. J. A. Nanoparticle Platform To Evaluate Bioconjugation and Receptor-Mediated Cell Uptake Using Cross-Linked Polyion Complex Micelles Bearing Antibody Fragments. *Biomacromolecules* **2016**, *17* (5), 1818−1833.
(31) Greene, M. K.; Richards, D. A.; Nogueira, J. C. F.; Campbell, K.; Smyth, P.; Fernández, M.; Scott, C. J.; Chudasama, V. Forming Next-Generation Antibody-Nanoparticle Conjugates through the Oriented Installation of Non-Engineered Antibody Fragments. *Chem. Sci.* **2018**, *9* (1), 79−87.
(32) Caporale, A.; Selis, F.; Sandomenico, A.; Jotti, G. S.; Tonon, G.; Ruvo, M. The LQSP Tetrapeptide Is a New Highly Efficient Substrate of Microbial Transglutaminase for the Site-specific Derivatization of Peptides and Proteins. *Biotechnol. J.* **2015**, *10* (1), 154−161.
(33) Steffen, W.; Ko, F. C.; Patel, J.; Lyamichev, V.; Albert, T. J.; Benz, J.; Rudolph, M. G.; Bergmann, F.; Streidl, T.; Kratzsch, P.; Boenitz-Dulat, M.; Oelschlaegel, T.; Schraeml, M. Discovery of a Microbial Transglutaminase Enabling Highly Site-Specific Labeling of Proteins. *J. Biol. Chem.* **2017**, *292* (38), 15622−15635.
(34) Lee, N. K.; Cho, S.; Kim, I.-S. Ferritin—a Multifaceted Protein Scaffold for Biotherapeutics. *Exp. Mol. Med.* **2022**, *54* (10), 1652−1657.
(35) Yoo, J. D.; Bae, S. M.; Seo, J.; Jeon, I. S.; Vadevoo, S. M. P.; Kim, S.-Y.; Kim, I.-S.; Lee, B.; Kim, S. Designed Ferritin Nanocages Displaying Trimeric TRAIL and Tumor-Targeting Peptides Confer Superior Anti-Tumor Efficacy. *Sci. Rep.* **2020**, *10* (1), No. 19997.
(36) Kim, G. B.; Sung, H.-D.; Nam, G.-H.; Kim, W.; Kim, S.; Kang, D.; Lee, E. J.; Kim, I.-S. Design of PD-1-Decorated Nanocages Targeting Tumor-Draining Lymph Node for Promoting T Cell Activation. *J. Controlled Release* **2021**, *333*, 328−338.
(37) Geninatti Crich, S.; Cadenazzi, M.; Lanzardo, S.; Conti, L.; Ruiu, R.; Alberti, D.; Cavallo, F.; Cutrin, J. C.; Aime, S. Targeting Ferritin Receptors for the Selective Delivery of Imaging and Therapeutic Agents to Breast Cancer Cells. *Nanoscale* **2015**, *7* (15), 6527−6533.
(38) Marrink, S. J.; Risselada, H. J.; Yefimov, S.; Tieleman, D. P.; de Vries, A. H. The MARTINI Force Field: Coarse Grained Model for Biomolecular Simulations. *J. Phys. Chem. B* **2007**, *111* (27), 7812−7824.
(39) Izadi, S.; Anandakrishnan, R.; Onufriev, A. V. Implicit Solvent Model for Million-Atom Atomistic Simulations: Insights into the Organization of 30-Nm Chromatin Fiber. *J. Chem. Theory Comput.* **2016**, *12* (12), 5946−5959.
(40) Eaton, D. L.; Wood, W. I.; Eaton, D.; Hass, P. E.; Hollingshead, P.; Wion, K.; Mather, J.; Lawn, R. M.; Vehar, G. A.; Gorman, C. Construction and Characterization of an Active Factor VIII Variant Lacking the Central One-Third of the Molecule. *Biochemistry* **1986**, *25* (26), 8343−8347.
(41) Paborsky, L. R.; Fendly, B. M.; Fisher, K. L.; Lawn, R. M.; Marks, B. J.; McCray, G.; Tate, K. M.; Vehar, G. A.; Gorman, C. M. Mammalian Cell Transient Expression of Tissue Factor for the Production of Antigen. *Protein Eng., Des. Sel.* **1990**, *3* (6), 547−553.
(42) Mastronarde, D. N. Automated Electron Microscope Tomography Using Robust Prediction of Specimen Movements. *J. Struct. Biol.* **2005**, *152* (1), 36−51.
(43) Punjani, A.; Rubinstein, J. L.; Fleet, D. J.; Brubaker, M. A. CryoSPARC: Algorithms for Rapid Unsupervised Cryo-EM Structure Determination. *Nat. Methods* **2017**, *14* (3), 290−296.
(44) Rohou, A.; Grigorieff, N. CTFFIND4: Fast and Accurate Defocus Estimation from Electron Micrographs. *J. Struct. Biol.* **2015**, *192* (2), 216−221.
(45) Meyerson, J. R.; Rao, P.; Kumar, J.; Chittori, S.; Banerjee, S.; Pierson, J.; Mayer, M. L.; Subramaniam, S. Self-Assembled Monolayers Improve Protein Distribution on Holey Carbon Cryo-EM Supports. *Sci. Rep.* **2014**, *4* (1), No. 7084.

(46) Goddard, T. D.; Huang, C. C.; Meng, E. C.; Pettersen, E. F.; Couch, G. S.; Morris, J. H.; Ferrin, T. E. UCSF ChimeraX: Meeting Modern Challenges in Visualization and Analysis. *Protein Sci.* **2018**, *27* (1), 14−25.

https://doi.org/10.1021/acs.bioconjchem.4c00020
Bioconjugate Chem. 2024, 35, 593−603